

Primordial black holes from slow phase transitions: a model-building perspective

Shinya Kanemura,^a Masanori Tanaka,^{a,b} and Ke-Pan Xie^c

^a*Department of Physics, Osaka University, Toyonaka, Osaka 560-0043, Japan*

^b*Center for High Energy Physics, Peking University, Beijing 100871, China*

^c*School of Physics, Beihang University, Beijing 100191, China*

E-mail: kanemu@het.phys.sci.osaka-u.ac.jp, tanaka@pku.edu.cn,
kpxie@buaa.edu.cn

ABSTRACT: We investigate the formation of primordial black holes (PBHs) through delayed vacuum decay during slow cosmic first-order phase transitions. Two specific models, the polynomial potential and the real singlet extension of the Standard Model, are used as illustrative examples. Our findings reveal that models with zero-temperature scalar potential barriers are conducive to the realization of this mechanism, as the phase transition duration is extended by the U-shaped Euclidean action. We find that the resulting PBH density is highly sensitive to the barrier height, with abundant PBH formation observed for sufficiently high barriers. Notably, the phase transition needs not to be ultra-supercooled (i.e. the parameter $\alpha \gg 1$), and the commonly used exponential nucleation approximation $\Gamma(t) \sim e^{\beta t}$ fails to capture the PBH formation dynamics in such models.

Contents

1	Introduction	1
2	Framework for calculation	2
2.1	Deriving the PBH profiles	2
2.2	The exponential approximation and beyond	5
3	The model with a polynomial potential	7
3.1	Model description and PBH formation	7
3.2	Comparison among different expansions of $S(t)$	11
4	The \mathbb{Z}_2-symmetric singlet extension of the SM	14
5	Conclusion	16
A	FOPT dynamics under the exponential approximation	18

1 Introduction

Due to their profound cosmological and astrophysical implications, primordial black holes (PBHs) have attracted significant research attention [1–4]. Those hypothetical black holes originate in the early Universe shortly after the Big Bang, long before the existence of stars and galaxies. Cosmic first-order phase transitions (FOPTs) provide a favorable environment for PBH formation: the Universe transitions from a higher energy false vacuum to a lower energy true vacuum via tunneling, resulting in the true vacuum bubbles nucleate and expand in the false vacuum background. This may lead to the formation of PBHs, if the bubble collisions compress a large amount of energy into a small volume [5–7], or if some false vacuum remnants form significant overdensities via delayed vacuum decay [8–28] or trapping fermions [29–47]. While FOPTs might be generic during the thermal history of the Universe [48], the formation of PBHs during such transitions is highly nontrivial. It typically imposes additional constraints on the temperature, strength, duration, and bubble expansion velocity of the FOPT, as well as the particle content of the underlying model. Depending on scenarios, the PBHs from FOPTs have various mass, spin, and abundance distributions.

In this work, we focus on the mechanism based on the delayed vacuum decay [11] (also see a similar scenario in Ref. [8]). During the FOPT, the energy stored in the false vacuum regions is released and converted to radiation energy. Because of the randomness of the vacuum tunneling process, the timing of bubble nucleation varies across Hubble patches. Some patches experience delayed nucleation compared to the average time, and

become overdense over time as they have larger vacuum energy fractions, whose density maintains a constant, while the overall Universe is dominated by radiation that dilutes its energy density via expansion. Those patches eventually decay and release vacuum energy to radiation energy, and when the overdensity reaches a certain threshold, the delayed-decay patches collapse into PBHs.

This mechanism has been extensively studied in the literature on its detailed calculations, applications, and phenomenology [12–25]. Most studies are agnostic about the underlying particle models, employing the FOPT parameters such as α and β/H_* as input parameters. In particular, the exponential nucleation rate approximation $\Gamma(t) \sim e^{\beta t}$ is commonly adopted. In this paper, we focus on the implementation of the mechanism in particle physics models beyond the Standard Model (SM), and for the first time analyze its general relationship with the scalar potential structure of the model. By investigating models that incorporate *zero-temperature potential barriers*, we find that such models typically exhibit a U-shaped Euclidean action $S_3(T)/T$, which results in slow FOPTs, conducive to delayed vacuum decay and hence PBH formation. The PBH abundance is very sensitive to the height of the zero-temperature barrier. We also confirm that the $\Gamma(t) \sim e^{\beta t}$ approximation is not suitable due to its reliance on the linear time-expansion of the Euclidean action, which fails to capture the characteristics of a U-shaped action in such models [49].

To illustrate our findings, we consider two concrete models. The first model utilizes a polynomial potential, serving as a prototype or toy model. The second model is the \mathbb{Z}_2 -preserving real singlet extension of the SM (dubbed as the \mathbb{Z}_2 -xSM), representing a realistic scenario concerning the first-order electroweak phase transition. In Section 2, we describe our calculation framework in detail, and also compare different approximation methods for the nucleation rate. Subsequently, we apply this framework to analyze the polynomial potential in Section 3 and the \mathbb{Z}_2 -xSM model in Section 4, presenting our main results. The conclusion will be given in Section 5.

2 Framework for calculation

2.1 Deriving the PBH profiles

In the early Universe, the scalar potential’s shape changes with temperature. Initially, the Universe occupies the minimum of the potential, known as the vacuum. However, below the critical temperature, the potential develops another deeper minimum, which becomes the true vacuum. The Universe remains stuck in the initial false vacuum due to a barrier that prevents a smooth transition to the global minimum. Thermal tunneling allows the Universe to transition to the true vacuum with a probability per unit volume and per unit time [50]

$$\Gamma(T) \sim T^4 \left(\frac{S(T)}{2\pi} \right)^{3/2} e^{-S(T)}, \quad (2.1)$$

where $S(T) = S_3(T)/T$, and $S_3(T)$ is the $O(3)$ -symmetric Euclidean action evaluated from the scalar potential. As the temperature T depends on cosmic time t , we can express the

action and decay rate as $S(t) = S(T(t))$ and $\Gamma(t) = \Gamma(T(t))$, respectively. Denoting t_c as the time corresponding to the critical temperature T_c where the two vacua are degenerate, we have $S(t_c) = \infty$ and $\Gamma(t_c) = 0$.

We now describe the evolution of the Universe in a FOPT. For a given Hubble patch, according to the first Friedmann equation, the Hubble constant is given by

$$H(t) = \frac{\dot{a}(t)}{a(t)} = \sqrt{\frac{8\pi}{3M_{\text{Pl}}^2}\rho(t)}, \quad (2.2)$$

where $M_{\text{Pl}} = 1.22 \times 10^{19}$ GeV is the Planck scale, $a(t)$ is the scale factor, and $\rho(t) = \rho_r(t) + \rho_v(t)$ is the energy density that can be decomposed into the radiation and vacuum components

$$\rho_r(t) = \frac{\pi^2}{30}g_*T^4(t), \quad \rho_v(t) = F(t)\Delta V(t), \quad (2.3)$$

where the factor g_* is the number of effective degrees of freedom, and $\Delta V(t)$ is the energy density difference between the false and true vacua, which is 0 for $t \leq t_c$ and positive for $t > t_c$. The false vacuum volume fraction is defined as

$$F(t) = \begin{cases} 1, & \text{if } t < t_d; \\ \exp\left\{-\frac{4\pi}{3}\int_{t_d}^t dt'\Gamma(t')a^3(t')\left[\int_{t'}^t dt''\frac{v_w}{a(t'')}\right]^3\right\}, & \text{if } t > t_d. \end{cases} \quad (2.4)$$

where t_d is the time that the Hubble patch starts to nucleate, and v_w is the bubble expansion velocity.

As the FOPT proceeds, $F(t)$ decreases from 1 to 0, and the vacuum energy is converted to radiation. This can be clearly seen from the variation of the second Friedmann equation,

$$\frac{d\rho_r}{dt} + 4H\rho_r = -\frac{d\rho_v}{dt}. \quad (2.5)$$

Given t_d , with the initial condition $\rho_r(t_c) = \pi^2g_*T_c^4/30$ and $\rho_v(t_c) = 0$, one is able to resolve Eqs. (2.2), (2.4), and (2.5) consistently by iteration, and obtain the evolutions of the physical observables, such as $T(t)$, $\rho_{r,v}(t)$, $H(t)$, and $F(t)$, etc. As mentioned before, t_d varies in different patches since vacuum tunneling is probabilistic. For simplicity, we categorize the Hubble patches into two types: normal ones and delayed-decay ones. Normal patches initiate nucleation after the Universe cools to the critical temperature, i.e. $t_d = t_c$, which is the most prevalent case. Delayed-decay patches, on the other hand, have a late nucleation time, i.e. $t_d > t_c$. We use the subscripts ‘‘out’’ and ‘‘in’’ to label the two types of patches and the corresponding physical observables, respectively. The normal patch can be resolved once the underlying particle model is set, while the delayed-decay patch is determined by one extra parameter t_d .

The delayed-decay patches form overdensities with respect to normal patches because the latter receive more radiation contributions, and $\rho_r \propto a^{-4}$ redshifts rapidly while $\rho_v \propto a^0$ remains a constant. The overdensity is defined as

$$\delta(t) = \frac{\rho_{\text{in}}(t)}{\rho_{\text{out}}(t)} - 1 = \frac{\rho_{r,\text{in}}(t) + \rho_{v,\text{in}}(t)}{\rho_{r,\text{out}}(t) + \rho_{v,\text{out}}(t)} - 1. \quad (2.6)$$

As time t increases from t_c , $\delta(t)$ increases from 0 to a maximum value, δ_{\max} , and then decreases back to zero as $t \rightarrow \infty$. If δ_{\max} exceeds a threshold value δ_c , the delayed-decay patch collapses into a PBH at t_{pbh} satisfying $\delta(t_{\text{pbh}}) = \delta_c$. In this paper, we take $\delta_c = 0.45$ as the PBH formation criterion [51, 52]. This criterion can be obtained under the assumption that the Universe is radiation dominant and that the overdensity region is spherically symmetric. If the overdensity region occurs due to vacuum energy, an inflationary expanding baby Universe is realized there [53–56], and the region appears to the outside observer as a PBH. As it has not been numerically shown what value of δ_c should be taken in such situations, we take the well-known value $\delta_c = 0.45$ as a benchmark in our study.

We can establish a mapping between t_d and δ_{\max} . Generally, δ_{\max} increases with t_d since a patch with later vacuum decay forms a larger energy contrast. However, the probability of “a patch remains in the false vacuum until t_d ” decreases rapidly as t_d increases. Thus, we infer that the smallest value of t_d allowing for collapse dominates the abundance of PBHs. This corresponds to the value of t_d where $\delta_{\max} = \delta_c$, and the moment when this maximum value is reached defines the PBH formation time t_{pbh} , specifically $\delta(t_{\text{pbh}}) = \delta_{\max} = \delta_c$. By this procedure, we can determine t_d and t_{pbh} simultaneously (note $t_{\text{pbh}} > t_d$). The resultant PBH mass is

$$m_{\text{pbh}} \approx \gamma V_{H,\text{in}}(t_{\text{pbh}}) \rho_{\text{in}}(t_{\text{pbh}}) \approx \gamma \times \frac{4\pi}{3} H_{\text{in}}^{-3}(t_{\text{pbh}}) \times \frac{3M_{\text{Pl}}^2}{8\pi} H_{\text{in}}^2(t_{\text{pbh}}), \quad (2.7)$$

where $V_H(t_{\text{pbh}}) = (4\pi/3)H_{\text{in}}^{-3}(t_{\text{pbh}})$ is the Hubble volume. The factor γ represents the ratio between the PBH mass and the Hubble mass. We here take $\gamma \approx 0.2$ [57].

To determine the abundance of PBHs, it is necessary to evaluate the probability of a patch nucleating at time t_d . That is to find a region with a Hubble volume $(4\pi/3)H_{\text{in}}^{-3}(t_{\text{pbh}})$ that remains bubble-free until t_d . Within the time interval $t_c < t < t_{\text{pbh}}$, this region has a volume of $(4\pi/3)[a_{\text{in}}(t)/a_{\text{in}}(t_{\text{pbh}})]^3 H_{\text{in}}^{-3}(t_{\text{pbh}})$, and the probability of no bubble formation in this region during the time interval $[t, t + dt]$ is given by

$$dP = 1 - \frac{4\pi}{3} \frac{a_{\text{in}}^3(t)}{a_{\text{in}}^3(t_{\text{pbh}})} \frac{\Gamma_{\text{in}}(t)}{H_{\text{in}}^3(t_{\text{pbh}})} dt \approx \exp \left\{ -\frac{4\pi}{3} \frac{a_{\text{in}}^3(t)}{a_{\text{in}}^3(t_{\text{pbh}})} \frac{\Gamma_{\text{in}}(t)}{H_{\text{in}}^3(t_{\text{pbh}})} dt \right\}. \quad (2.8)$$

Consequently, the probability of no bubble nucleation during the time interval $t \in [t_c, t_d]$ is given by

$$P(t_d) = \prod dP = \exp \left\{ -\frac{4\pi}{3} \int_{t_c}^{t_d} dt \frac{a_{\text{in}}^3(t)}{a_{\text{in}}^3(t_{\text{pbh}})} H_{\text{in}}^{-3}(t_{\text{pbh}}) \Gamma_{\text{in}}(t) \right\}. \quad (2.9)$$

This expression demonstrates that $P(t_d)$ is exponentially dependent on t_d , emphasizing the significance of setting the PBH formation time and mass through $\delta(t_{\text{pbh}}) = \delta_{\max} = \delta_c$. This lower limit on t_d governs the PBH density.

With $P(t_d)$ in hand, we can calculate ρ_{pbh} . Suppose the numbers of the delayed-decay and normal Hubble patches are N_{in} and N_{out} , respectively, and then the energy density of PBH is

$$\rho_{\text{pbh}} = \frac{N_{\text{in}} m_{\text{pbh}}}{N_{\text{out}} V_{H,\text{out}}(t_{\text{pbh}}) + N_{\text{in}} V_{H,\text{in}}(t_{\text{pbh}})}, \quad (2.10)$$

where V_H is again the Hubble volume. The delayed-decay probability $P(t_d)$ implies

$$P(t_d) = \frac{N_{\text{in}}}{N_{\text{in}} + N_{\text{out}}}, \quad (2.11)$$

and substituting this relation back to Eq. (2.10) yields

$$\rho_{\text{pbh}} = \frac{P(t_d) \cdot m_{\text{pbh}}}{(1 - P(t_d))V_{H,\text{out}} + P(t_d)V_{H,\text{in}}} \approx P(t_d) \frac{m_{\text{pbh}}}{V_{H,\text{out}}}, \quad (2.12)$$

where the approximate equality holds because $P(t_d) \ll 1$. The present-day energy density of PBHs is given by $\rho_{\text{pbh}}^0 = \rho_{\text{pbh}} s_0 / s$, where $s \approx 2\pi^2 g_{*s} T_{\text{out}}^3(t_{\text{pbh}}) / 45$ and $s_0 \approx 2891.2 \text{ cm}^{-3}$ [58] the entropy at PBH formation and today, respectively. The relic abundance of PBHs can be expressed as $\Omega_{\text{pbh}} = \rho_{\text{pbh}}^0 / \rho_0$, where $\rho_0 = (3M_{\text{Pl}}^2 / 8\pi) H_0^2$ with $H_0 \approx 67.4 \text{ km}/(\text{s} \cdot \text{Mpc})$ the current Hubble constant [58]. We further define the PBH fraction of dark matter as

$$f_{\text{pbh}} = \frac{\Omega_{\text{pbh}}}{\Omega_{\text{dm}}}, \quad (2.13)$$

where $\Omega_{\text{dm}} h^2 \approx 0.12$ is the dark matter relic abundance.

We have described our framework to determine the formation time, mass, and relic abundance of PBHs. The formalism applies to general particle models with various shapes of potentials. Our calculation disregards the FOPT reheating effect, assuming a constant product of temperature (T) and scale factor (a). This simplification may not hold for ultra-supercooled FOPTs with the parameter $\alpha \gg 1$, where the Universe's temperature can be increased by a factor of approximately $(1 + \alpha)^{1/4}$ after the transition. However, our analysis focuses only on the mild-supercooled case when α is moderate, making the reheating effect negligibly small. More discussions on calculations involving very strong FOPTs can be found in Refs. [16, 17].

2.2 The exponential approximation and beyond

Once the underlying particle model is built, one is able to derive $S(t)$ and also $\Gamma(t)$, and proceed the calculation as described in Section 2.1. To simplify the calculation, most previous studies have chosen to expand the action at a specific moment t_* ,

$$S(t) \approx S(t_*) - \beta(t - t_*) + \frac{\zeta^2}{2}(t - t_*)^2 + \dots, \quad (2.14)$$

and have written down

$$\Gamma(t) \approx \Gamma_* e^{\beta(t-t_*) - \frac{\zeta^2}{2}(t-t_*)^2 + \dots}, \quad (2.15)$$

where T_* is the temperature at t_* , and $\Gamma_* = T_*^4 (S(t_*) / (2\pi))^{3/2}$. Here the Taylor expansion coefficients are

$$\beta = -\left. \frac{dS}{dt} \right|_*, \quad \zeta^2 = \left. \frac{d^2 S}{dt^2} \right|_*, \quad (2.16)$$

or they can be rewritten in the dimensionless forms and transferred into the derivatives on temperature, which are more explicitly derived from the particle model:

$$\frac{\beta}{H_*} = T_* \left. \frac{dS}{dT} \right|_*, \quad \left(\frac{\zeta}{H_*} \right)^2 = T_*^2 \left. \frac{d^2 S}{dT^2} \right|_* + \left(1 + \left. \frac{d \ln H}{d \ln T} \right|_* \right) \frac{\beta}{H_*}, \quad (2.17)$$

where H_* is the Hubble constant at t_* , and $S(T) = S_3(T)/T$.

Regarding the expansion Eq. (2.14), the commonly used approach is to consider only the linear β -term, leading to the exponential nucleation rate approximation $\Gamma(t) \approx \Gamma_* e^{\beta(t-t_*)}$, where β^{-1} is interpreted as the time scale of the phase transition. Therefore β/H_* can be understood as the ratio of Hubble time scale to FOPT duration. Besides β/H_* , there is another important parameter α describing the strength of the FOPT, defined as

$$\alpha = \left(\Delta V(t_*) - T(t_*) \frac{\partial \Delta V}{\partial T} \Big|_* \right) / \rho_r(t_*), \quad (2.18)$$

i.e. the ratio of phase transition latent heat to the radiation energy density, evaluated in the normal patches. The parameters α and β/H_* , together with the transition temperature T_* and bubble wall velocity v_w , can be used to calculate other observables of the FOPT dynamics, such as the stochastic gravitational wave (GW) spectrum [48, 59–61].

As for the expansion moment t_* , there are typically two choices. One is the nucleation time t_n , the moment that the bubble number in the normal patch reaches 1, i.e.

$$N(t_n) = \int_{t_c}^{t_n} dt' \frac{\Gamma(t')}{H^3(t')} = 1. \quad (2.19)$$

The other is the percolation time t_p , which is the moment when the bubbles in the normal patch form an infinite connecting cluster, i.e., $F(t_p) = 0.71$ [62]. In general $t_p > t_n$, and when the FOPT is prompt ($\beta/H_* \gg 1$) and moderate ($\alpha \lesssim 1$), $t_p \approx t_n$. However, if the FOPT is very strong or lasts for a long time, t_p differs significantly from t_n . In that case, it is proposed to adopt $t_* = t_p$, and replace β/H_* with $(8\pi)^{1/3} v_w / (H_* \bar{R})$ in the GW calculation, where \bar{R} is the mean separation of bubbles [49, 63, 64], which can be adopted as $[n_b(t_*)]^{-1/3}$, with

$$n_b(t) = \int_{t_c}^t dt' F(t') \Gamma(t') \frac{a^3(t')}{a^3(t)}, \quad (2.20)$$

the bubble number density in the normal patches. Furthermore, one should also check the FOPT completion condition [49, 65]

$$3H(t_p) + \frac{d \ln F(t)}{dt} \Big|_p < 0, \quad (2.21)$$

such that the physical volume of the false vacuum is decreasing at percolation.

The exponential approximation is widely used in FOPT research and is generally effective. It is also commonly employed in the study of PBH formation from delayed vacuum decay [11–15, 17–26]. However, PBH formation predominantly occurs in the small β/H_* region, which corresponds to slow FOPTs with prolonged durations. For instance, previous studies indicate $\beta/H_* \lesssim 10$ for abundant PBH formation [11, 16, 17]. When the first-order expansion coefficient β of $S(t)$ is small, it becomes necessary to check if truncating the expansion Eq. (2.14) at linear order provides a satisfactory approximation. This can be determined by examining whether the ratio of the second-order expansion to the first-order one, $|\zeta^2(t-t_*)^2/2|/|\beta(t-t_*)|$, is much less than 1 during the FOPT. This is equivalent to checking

$$\frac{1}{2} \left| \left(1 + \frac{d \ln H}{d \ln T} \Big|_* + \frac{d \ln S'}{d \ln T} \Big|_* \right) H_*(t-t_*) \right| \ll 1, \quad (2.22)$$

where S' represents dS/dT .

The factor $H_*(t - t_*)$ roughly measures the duration of FOPT over the Hubble time scale, and according to the calculations in Appendix A, it can be replaced by $\mathcal{O}(10) \times (\beta/H_*)^{-1}$. In addition, we can generally assume $H \propto T^n$ and $S \propto T^r$ near T_* , and then Eq. (2.22) reduces to

$$|n + r| \ll \mathcal{O}(0.2) \times \frac{\beta}{H_*}. \quad (2.23)$$

PBH formation requires the right-hand side (r.h.s.) of Eq. (2.23) to be $\sim 0.2 \times 10 \sim 2$. However, in ultra-supercooled and mild FOPTs with vacuum and radiation domination, the left-hand side (l.h.s.) typically takes values of $n \approx 0$ and $n \approx 2$ respectively, while a realistic particle model usually has $r > 1$. Consequently, it is challenging to satisfy the exponential approximation condition in the parameter space favored by the PBH mechanism. If the l.h.s. is not sufficiently small, including additional terms in the expansion, such as the quadratic ζ -term [16], becomes necessary.

In our study, we directly compare the results obtained using three different methods for $\Gamma(t)$: (1) the full expression, (2) the first-order expansion with only the β -term (exponential approximation), and (3) the second-order expansion with both the β - and ζ -terms. We find that the first-order expansion is inadequate, and it results in significant differences in PBH mass and abundance compared to the results obtained from the full expression case. By including the quadratic term, the results are much improved and closer to those of the full expression case, although visible differences still persist, particularly for relatively mild FOPTs. Our results demonstrate the importance of utilizing the full expressions for $\Gamma(t)$ in the PBH formation calculation in realistic models.

3 The model with a polynomial potential

3.1 Model description and PBH formation

Let ϕ be the scalar that triggers the FOPT, and $V(\phi, T)$ its potential in the thermal bath of the early Universe at temperature T , we parametrize the potential as

$$V(\phi, T) = \frac{1}{2} \left(\frac{\mu_3 w - m_\phi^2}{2} + cT^2 \right) \phi^2 - \frac{\mu_3}{3} \phi^3 + \frac{m_\phi^2}{8w^2} \left(1 + \frac{\mu_3 w}{m_\phi^2} \right) \phi^4, \quad (3.1)$$

and restrict the value of μ_3 to be within the range

$$\frac{m_\phi^2}{w} < \mu_3 < \frac{3m_\phi^2}{w}. \quad (3.2)$$

At $T = 0$, $V(\phi, 0)$ has two minima at $\phi = 0$ and w , and the latter is the true vacuum. The ϕ boson mass square is $m_\phi^2 = d^2V(\phi, 0)/d\phi^2|_{\phi=w}$. Between the two minima, there is a local maximum at $\phi = w_b$, corresponding to the zero-temperature barrier

$$V(w_b, 0) = \frac{m_\phi^2 w^2}{24} \left(3 + \frac{\mu_3 w}{m_\phi^2} \right) \left(1 - \frac{2}{1 + w\mu_3/m_\phi^2} \right)^3. \quad (3.3)$$

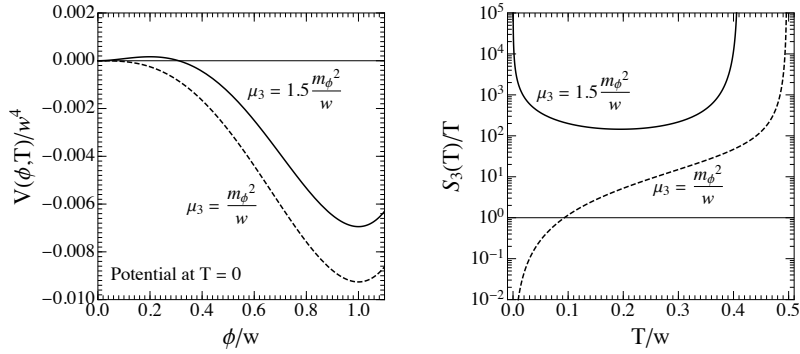


Figure 1. Left: the zero-temperature potentials. Right: the $S_3(T)/T$ curves. $m_\phi = 300$ MeV, $w = 900$ MeV, and $c = 0.11$, while μ_3 takes $m_\phi^2/w = 100$ MeV or $1.5m_\phi^2/w = 150$ MeV.

It exists when $\mu_3 > m_\phi^2/w$. If we increase μ_3 , the barrier height increases accordingly, and $V(w, 0)$ is also shifted. When μ_3 reaches $3m_\phi^2/w$, the $\phi = w$ vacuum becomes degenerate with the $\phi = 0$ one. Therefore, we consider μ_3 in the range in Eq. (3.2) to ensure there is a barrier at zero-temperature, and $\phi = w$ is the true vacuum.

The finite temperature correction to the potential is described by the c -term in Eq. (3.1), where we only include the leading T^2 -terms of the thermal integrals coming from light degrees of freedom. The subdominant $-c'T\phi^3$ term from the bosonic degrees of freedom is omitted. The Universe stays in the false vacuum $\phi = 0$ initially and it acquires a probability of decaying to the true vacuum when $T < T_c$. The decay rate $\Gamma(T) \sim e^{-S_3(T)/T}$ is defined in Eq. (2.1). At $T = T_c$, the two vacua are degenerate and hence $S_3(T_c) = \infty$; when the Universe cools down from T_c , $S_3(T)/T$ also decreases. If there exists a zero-temperature barrier, then $S_3(T)$ approaches a finite value for $T \rightarrow 0$, resulting in $\lim_{T \rightarrow 0} S_3(T)/T = \infty$. Therefore, in such a case we have a U-shaped $S(T) = S_3(T)/T$ curve, which efficiently suppresses the vacuum decay rate and hence results in a long FOPT. To illustrate this, we adopt $m_\phi = 300$ MeV, $w = 900$ MeV, and $c = 0.11$ as a benchmark, and test two different μ_3 values: $m_\phi^2/w = 100$ MeV and $1.5m_\phi^2/w = 150$ MeV. The former corresponds to vanishing barrier at zero-temperature and hence $S_3(T)/T \rightarrow 0$ when $T \rightarrow 0$, while the latter corresponds to a barrier that results in a U-shaped $S_3(T)/T$ curve, as clearly illustrated in Fig. 1. For the $S_3(T)/T$ calculation, we have used the semi-analytical expression [66]

$$\frac{S_3(T)}{T} \approx \frac{123.48(\mu^2 + cT^2)^{3/2}}{2^{3/2}T\mu_3^2} f\left(\frac{9(\mu^2 + cT^2)\lambda}{2\mu_3^2}\right), \quad (3.4)$$

where

$$\mu^2 = \frac{\mu_3 w - m_\phi^2}{2}, \quad \lambda = \frac{\mu_3 w + m_\phi^2}{2w^2}, \quad f(u) = 1 + \frac{u}{4} \left[1 + \frac{2.4}{1-u} + \frac{0.26}{(1-u)^2} \right]. \quad (3.5)$$

The approximation works well when $u \in [0, 1]$. More discussions on the FOPT dynamics on the U-shaped $S_3(T)/T$ can be found in Refs. [67, 68], while here we only focus on the impacts on PBH formation.

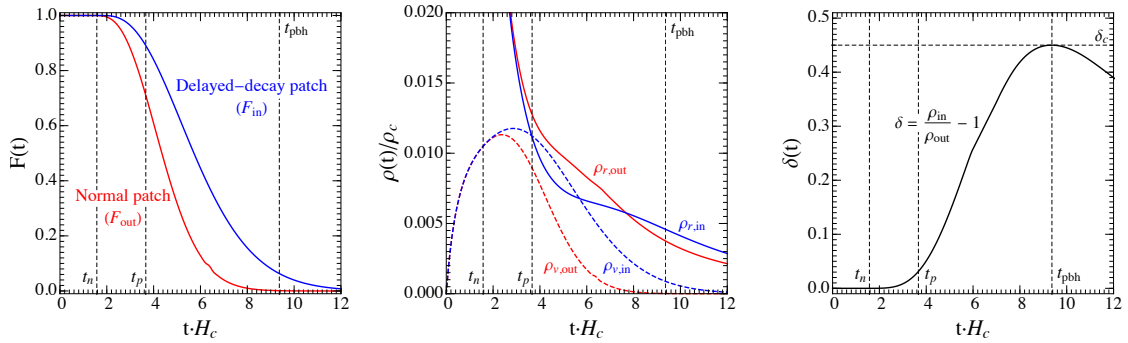


Figure 2. The FOPT and PBH profiles for $m_\phi = 300$ MeV, $w = 900$ MeV, $c = 0.11$, and $\mu_3 = 154.1$ MeV. t_n , t_p , and t_{pbh} are the nucleation, percolation, and PBH formation time, respectively. H_c and ρ_c denote the Hubble constant and radiation energy density at t_c , respectively. Left: the false vacuum fraction $F(t)$. Middle: the energy components $\rho_{r,v}(t)$. Right: the overdensity $\delta(t)$.

For a given set of $\{m_\phi, w, \mu_3, c\}$, we apply the methodology outlined in Section 2.1 to obtain the FOPT profiles and calculate the PBH formation. We set $v_w = 1.0$ as a fixed parameter. An illustrative example is presented in Fig. 2 with $\mu_3 = 154.1$ MeV. In the left panel, we depict the evolution of the false vacuum fraction $F(t)$. From the figure it can be clearly seen that delayed-decay patches initiate nucleation at later times compared to normal patches. Consequently, this results in distinct energy component evolutions, as shown in the middle panel. In both cases, the vacuum energy $\rho_v(t)$ is converted into radiation energy $\rho_r(t)$; however, delayed-decay patches exhibit higher values of $\rho_r(t)$ at later times. The right panel displays the overdensity $\delta(t)$, which progressively increases with time until it reaches the maximum value $\delta_{\text{max}} = \delta_c$. This defines the PBH formation time $t_{\text{pbh}} = 4.70 \times 10^{-5}$ s. The corresponding PBH mass is $m_{\text{pbh}} = 2.72 \times 10^{33}$ g $= 1.37 M_\odot$, where M_\odot is the solar mass. For reference, the nucleation time t_n and percolation time t_p of the normal patches are also indicated in the figures, and we can see that $t_{\text{pbh}} > t_p > t_n$, which is a typical feature of this PBH mechanism.

In Fig. 3, we present the scan results in the c - μ_3 plane, with fixed values of $m_\phi = 300$ MeV and $w = 900$ MeV. By varying μ_3 and c around the center point at $\mu_3 = 154$ MeV and $c = 0.11$, we explore the parameter space for FOPT and PBH formation. We observe that the PBH fraction f_{pbh} is highly sensitive to these parameters, exhibiting a narrow band where it varies from 10^{-100} (the white dotted line) to $\sim 10^7$ (the upper edge of the color shaded region). This variation occurs within a small range, with μ_3 changing by only about $\sim 0.6\%$ and c changing by approximately $\sim 9\%$. Therefore, f_{pbh} is most sensitive to μ_3 , which describes the height of the zero-temperature potential barrier. This can be understood as the duration of FOPT is determined by the barrier, and f_{pbh} is extremely sensitive to this duration, which is a main feature of the PBH formation mechanism through delayed vacuum decay. The resulting PBHs form at around 10^{-5} s after the Big Bang, and have a mass of $\sim 10^{33}$ g ($\sim M_\odot$). Within this mass region, f_{pbh} is constrained to be $\lesssim 10^{-2}$

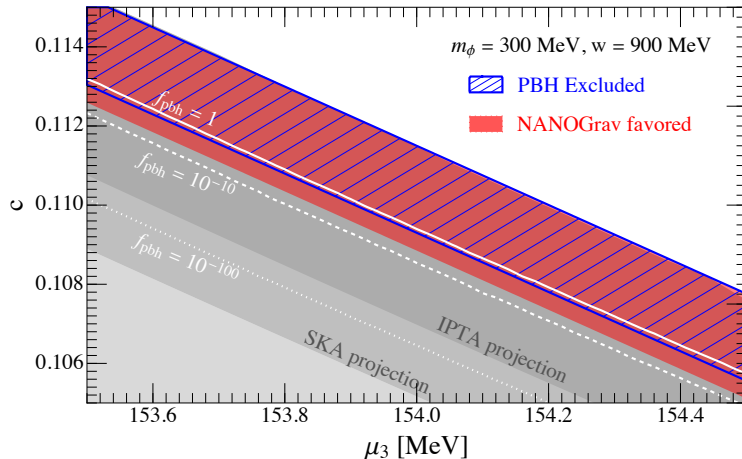


Figure 3. The scan result in the c - μ_3 plane for $m_\phi = 300$ MeV and $w = 900$ MeV. The white region cannot realize the FOPT. The white solid, dashed, and dotted lines represent $f_{\text{pbh}} = 1$, 10^{-10} , and 10^{-100} , respectively. The red, gray, and lighter gray regions correspond to the parameter space that produces GWs favored by the NANOGrav excess, reached by future IPTA and SKA, respectively. The blue mesh region is excluded by microlensing experiments.

f_{pbh}	T_*	α	β/H_*	$\frac{(8\pi)^{1/3}v_w}{H_*\bar{R}}$
10^{-100}	184 MeV _n , 155 MeV _p	0.37 _n , 0.99 _p	46 _n , -29 _p	3.0 _n , 14 _p
10^{-10}	177 MeV _n , 143 MeV _p	0.46 _n , 1.5 _p	30 _n , -53 _p	3.0 _n , 8.4 _p
1	174 MeV _n , 137 MeV _p	0.46 _n , 1.9 _p	21 _n , -65 _p	3.0 _n , 6.7 _p

Table 1. The FOPT parameters corresponding to the scan in Fig. 3. The subscript “ n ” and “ p ” represent the values derived at nucleation (t_n) or percolation (t_p), respectively.

due to microlensing observations [1], and the blue mesh region is already excluded.

We evaluate the FOPT parameters, namely α , β/H_* , and $(8\pi)^{1/3}v_w/(H_*\bar{R})$, and observe that their contours closely align with those of f_{pbh} . To maintain clarity in the figure, we present the corresponding FOPT parameter values for different f_{pbh} in Table 1 instead of showing more contours in Fig. 3. We note that α at t_p tends to be larger than at t_n due to the greater dilution of radiation energy, as $t_p > t_n$. We do not have $\alpha \gg 1$, and hence the FOPT is not very strong. Regarding parameters related to the FOPT duration, we find that β/H_* at t_n and $(8\pi)^{1/3}v_w/(H_*\bar{R})$ at t_p decrease with longer FOPT durations. Conversely, $(8\pi)^{1/3}v_w/(H_*\bar{R})$ at t_n remains insensitive to parameter variations, while β/H_* at t_p can even become negative. The reasons for these observations will be discussed in the following subsection, and we will demonstrate that $(8\pi)^{1/3}v_w/(H_*\bar{R})$ at t_p can measure the ratio of Hubble time to FOPT duration.

The GWs generated by the FOPT are computed using numerical formulae [59], and their spectral peak falls within the 10 – 100 nHz range. This may provide an explanation for the recent excess observed in pulsar timing array (PTA) experiments, such

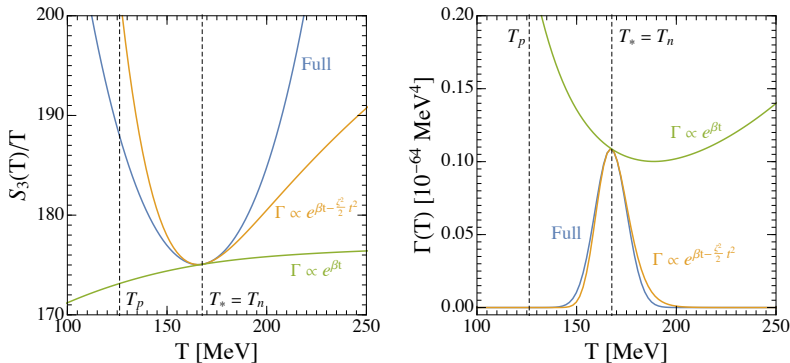


Figure 4. The evolutions of $S(T) = S_3(T)/T$ (left) and $\Gamma(T)$ (right), for different treatments: full expression (blue), quadratic expansion (orange), and linear expansion (green). $m_\phi = 300$ MeV, $w = 900$ MeV, $c = 0.11$, and $\mu_3 = 154.1$ MeV.

as NANOGrav [69], CPTA [70], EPTA [71], and PPTA [72]. Following the analysis conducted by the NANOGrav collaboration [73], we define “favored by the data” as a GW spectrum that matches the first 14 frequency bins of the NANOGrav-15yr dataset, highlighting this parameter space in red of Fig. 3. The parameter spaces accessible to future PTA experiments, such as IPTA [74] and SKA [75], are depicted in gray and lighter gray shades, respectively. Note that while much of the parameter space capable of explaining the NANOGrav excess has been ruled out by PBH detections, a narrow region remains unexplored, awaiting further investigation. We refrain from delving into the interplay between the PTA data, the FOPT, and PBHs, as the primary focus of this study is the relationship between the structure of particle models and PBH formation.¹

3.2 Comparison among different expansions of $S(t)$

In this subsection, we discuss different treatments of the Euclidean action $S(t)$: linear and quadratic approximations, and the full expression. To begin, we need to determine an appropriate expansion point t_* . Although the nucleation moment t_n and percolation moment t_p are potential choices, the previous subsection revealed that the region of parameter space where PBH formation is abundant has a negative value of β/H_* at t_p . This makes it unsuitable for expansion since it corresponds to a decreasing $\Gamma(t) \sim e^{\beta t}$ at the linear level approximation. Therefore, we select t_n as our expansion point.

Assuming parameters $m_\phi = 300$ MeV, $w = 900$ MeV, $c = 0.11$, and $\mu_3 = 154.1$ MeV, Fig. 4 displays the evolutions of the Euclidean action and vacuum decay rate, with the argument switched to temperature for convenience. The left panel shows that the three treatments intersect at T_n , but when T deviates from T_n , they exhibit distinct shapes, particularly the linear approximation. We now also easily understand why β/H_* at T_p is

¹For more discussions on the MeV-scale FOPT explanation of the PTA data, see Refs. [19, 76–92] and the references therein. Due to the extensive literature on this topic, we have only included those directly relevant to the June 2023 PTA excess announcement.

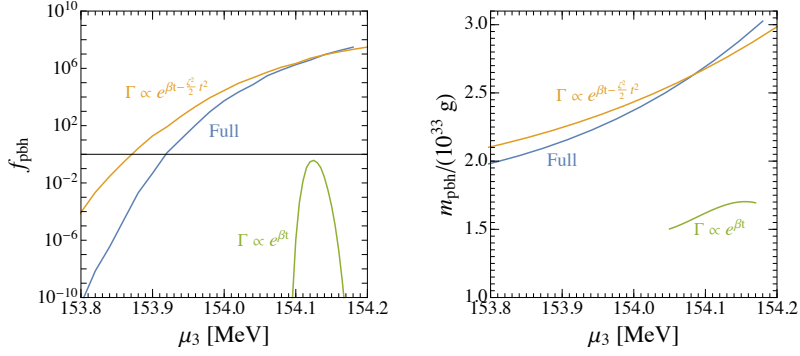


Figure 5. The curves of f_{pbh} (left) and m_{pbh} (right), scanning over μ_3 for different treatments of $S(t)$. $m_\phi = 300$ MeV, $w = 900$ MeV, and $c = 0.11$ are fixed.

negative: the full $S(T) = S_3(T)/T$ is U-shaped, and hence when the bubbles percolate at late time, dS/dT will become negative. The discrepancy in $S(T)$ results in differences in $\Gamma(T)$, as illustrated in the right panel. The exponential nucleation rate approximation fails completely in capturing the peak shape of the decay rate originating from the U-shaped action, whereas the quadratic approximation is much closer to the full expression, albeit with some visible differences. As a result, both the quadratic approximation and the full expression yield $m_{\text{pbh}} \sim 2.7 \times 10^{33}$ g ($\sim 1.36 M_\odot$) and $f_{\text{pbh}} \sim 2 \times 10^6$, while the linear approximation has $m_{\text{pbh}} \sim 1.6 \times 10^{34}$ g ($\sim 8.1 M_\odot$) and $f_{\text{pbh}} \sim 10^{-6}$.

The behavior of the linear and quadratic approximations can be understood by assuming $H \propto T^n$ near T_* , then

$$t - t_* = \int_T^{T_*} \frac{dT'}{T'H(T')} \xrightarrow{H \propto T^n} \begin{cases} \frac{1}{H_*} \frac{1}{n} \left[\left(\frac{T_*}{T} \right)^n - 1 \right], & n \neq 0; \\ \frac{1}{H_*} \log \left(\frac{T_*}{T} \right), & n = 0. \end{cases} \quad (3.6)$$

and hence Eq. (2.14) can also be treated as an expansion on temperature T , and we can have

$$S(T) - S(T_*) \approx \begin{cases} -\frac{1}{n} \frac{\beta}{H_*} \left[\left(\frac{T_*}{T} \right)^n - 1 \right] + \frac{1}{2n^2} \left(\frac{\zeta}{H_*} \right)^2 \left[\left(\frac{T_*}{T} \right)^n - 1 \right]^2, & n \neq 0; \\ -\frac{\beta}{H_*} \log \left(\frac{T_*}{T} \right) + \frac{1}{2} \left(\frac{\zeta}{H_*} \right)^2 \left[\log \left(\frac{T_*}{T} \right) \right]^2, & n = 0, \end{cases} \quad (3.7)$$

up to quadratic approximation level. Eq. (3.7) gives

$$\left. \frac{d^2 S}{dT^2} \right|_* \approx \frac{1}{T_*^2} \left[-(1+n) \left(\frac{\beta}{H_*} \right) + \left(\frac{\zeta}{H_*} \right)^2 \right]. \quad (3.8)$$

Since typically $n \in [0, 2]$, the linear approximation always has $d^2 S/dT^2|_* < 0$, which is qualitatively different from the full U-shaped expression that has $d^2 S/dT^2|_* > 0$ as

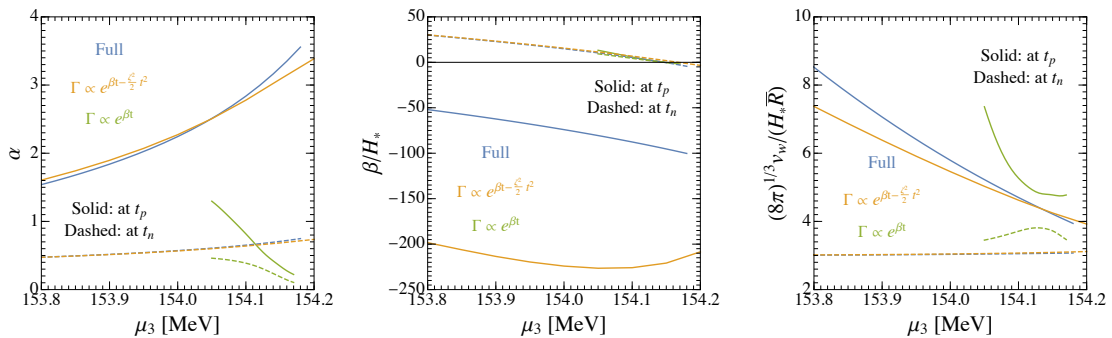


Figure 6. The curves of α_{pbh} (left), β/H_* (middle), and $(8\pi)^{1/3}v_w/(H_*\bar{R})$ (right), scanning over μ_3 for different treatments of $S(t)$. The same parameter setup as Fig. 5.

illustrated in Fig. 4. Such a discrepancy is not pronounced when the FOPT is prompt, as it completes near T_* . However, for PBH formation during a prolonged FOPT, the completion temperature deviates from T_* . This deviation leads to a significant distinction between the full $S(T)$ and its linear time expansion. Therefore, the exponential approximation $\Gamma(t) \sim e^{\beta t}$ cannot be applied to calculate PBH formation in scalar potentials with zero-temperature barriers when considering delayed vacuum decay. It's worth noting that this argument also applies to more general models with $S(T) \propto T^r$ and $r > 1$.

To further explore the differences among the three treatments, we maintain $m_\phi = 300$ MeV, $w = 900$ MeV, and $c = 0.11$, while varying μ_3 , and derive the curves of f_{pbh} and m_{pbh} in Fig. 5. The quadratic approximation exhibits a similar trend to the full expression and provides a close quantitative match in the large μ_3 region. However, for small μ_3 , the values of f_{pbh} can differ by several orders of magnitude. In contrast, the linear approximation yields entirely different curves. This discrepancy arises because the decay rate from the linear approximation is generally higher than the other two treatments, as illustrated in the right panel of Fig. 4. Therefore, it results in faster FOPTs, earlier PBH formation, lower values of f_{pbh} , t_{pbh} , and m_{pbh} .

We obtain the FOPT parameters α , β/H_* , and $(8\pi)^{1/3}v_w/(H_*\bar{R})$ at t_n and t_p , and present their dependence on μ_3 in Fig. 6. The left panel demonstrates the FOPT is mild in three different treatments. In the middle panel, we observe that β/H_* derived at t_n or t_p becomes negative for sufficiently large μ_3 , indicating it cannot be interpreted as a ratio of time scales. Conversely, the right panel demonstrates that $(8\pi)^{1/3}v_w/(H_*\bar{R})$ at t_p is positive and decreases with increasing FOPT duration in both the full expression and quadratic approximation cases. Therefore, it serves as a measure of the ratio between the Hubble time and the FOPT time scales.

Before closing this subsection, we emphasize the importance of verifying Eq. (2.21) when studying the formation of PBHs resulting from delayed vacuum decay. The FOPTs being considered here have a long duration, necessitating the confirmation of their completion. For instance, in Figs. 5 and 6, the curves representing the full expression evaluation

end at $\mu_3 \approx 154.18$ MeV, indicating that the FOPT cannot be fully accomplished beyond this point. If Eq. (2.21) is not satisfied, the physical volume of the false vacuum does not decrease at percolation, even if the volume fraction decreases; consequently, the FOPT remains incomplete [65].

4 The \mathbb{Z}_2 -symmetric singlet extension of the SM

This section discusses a more complicated and realistic model with double-field FOPT dynamics: the \mathbb{Z}_2 -symmetric xSM [93–95]. The scalar sector contains the SM Higgs doublet H and a \mathbb{Z}_2 -odd real gauge singlet s , and the joint potential at finite temperature can be written as

$$V(h, s, T) \approx \frac{1}{2} (\mu_h^2 + c_h T^2) h^2 + \frac{1}{2} (\mu_s^2 + c_s T^2) s^2 + \frac{\lambda_h}{4} h^4 + \frac{\lambda_s}{4} s^4 + \frac{\lambda_{hs}}{2} h^2 s^2, \quad (4.1)$$

where h and s are the neutral Higgs and singlet background field, respectively, and the coefficients

$$c_h = \frac{3g^2 + g'^2}{16} + \frac{y_t^2}{4} + \frac{\lambda_h}{2} + \frac{\lambda_{hs}}{12}, \quad c_s = \frac{\lambda_s}{4} + \frac{\lambda_{hs}}{3}, \quad (4.2)$$

are derived from the high-temperature expansion of the thermal collections, with g , g' , and y_t the $SU(2)_L$, $U(1)_Y$ gauge couplings, and the top Yukawa, respectively.²

We require $\lambda_h > 0$, $\lambda_s > 0$ and $\sqrt{\lambda_h \lambda_s} + \lambda_{hs} > 0$ to ensure the potential bounded from below, and

$$\mu_h^2 < 0, \quad \mu_s^2 < 0, \quad \lambda_h \mu_s^2 > \lambda_{hs} \mu_h^2, \quad \lambda_s \mu_h^2 > \lambda_{hs} \mu_s^2, \quad -\frac{\mu_h^4}{\lambda_h} < -\frac{\mu_s^4}{\lambda_s}, \quad (4.3)$$

such that at $T = 0$ there exists two local minima at $(h, s) = (v, 0)$ and $(0, w)$, with $v = \sqrt{-\mu_h^2/\lambda_h}$ and $w = \sqrt{-\mu_s^2/\lambda_s}$, and the former is the true vacuum, preserving the \mathbb{Z}_2 symmetry. The two minima are separated by a tree-level barrier induced by the λ_{hs} term. Since s does not acquire a vacuum expectation value at zero-temperature, it does not mix with h , and the physical masses of the scalars can be easily obtained as,

$$m_h^2 = -2\mu_h^2, \quad m_s^2 = \mu_s^2 + \lambda_{hs} v^2. \quad (4.4)$$

Given $m_h = 125$ GeV and $v = 246$ GeV, we only have three free parameters, which can be adopted as $\{m_s, \lambda_{hs}, \lambda_s\}$. Note that $m_s > m_h/2$ is required by phenomenology to evade the $h \rightarrow ss$ bound from collider experiments.

It is well-known that when $T > 0$ the \mathbb{Z}_2 -symmetric xSM can realize a two-step phase transition via the trajectory $(0, 0) \rightarrow (0, w_*) \rightarrow (v_*, 0)$, in which the second step is a first-order electroweak phase transition. Under the thermal potential Eq. (4.1), this is the only possible FOPT pattern, and its necessary condition is [97]

$$\frac{c_s}{c_h} < \frac{\mu_s^2}{\mu_h^2} < \frac{\sqrt{\lambda_s}}{\sqrt{\lambda_h}} < \frac{\lambda_{hs}}{\lambda_h}, \quad (4.5)$$

²Here we follow the conventions from Ref. [96], and the definition of λ_{hs} might differ from some references by a factor of 2. It is shown that including the T^2 -terms yields very similar results compared with the full one-loop calculation [96].

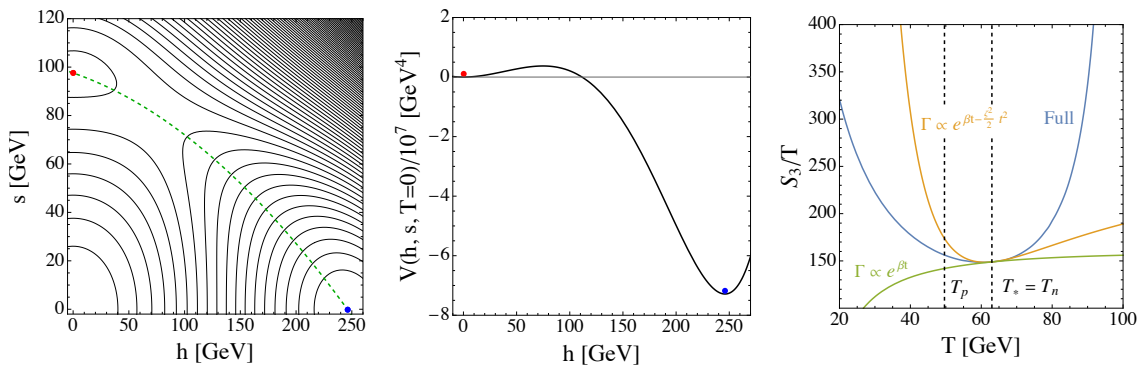


Figure 7. Left: the zero-temperature potential contours $V(h, s, 0)$, with the blue and red points denoting the true and false vacua, respectively. Middle: the field value along the green dashed line of the left panel. Right: the $S_3(T)/T$ curves for different treatments. The parameters are adopted as $m_s = 218$ GeV, $\lambda_s = 2$, and $\lambda_{hs} = 1.108$.

derived from the existence condition of T_c . Within this region, we resolve the FOPT dynamics of the model with the assistance of the Python package `cosmoTransitions` [98], which helps to evaluate $S_3(T)/T$. In Fig. 7, the left panel displays the contours of the potential $V(h, s, T)$ at $T = 0$, with fixed values of $m_s = 218$ GeV, $\lambda_s = 2$, and $\lambda_{hs} = 1.108$. Two distinct local minima, located at $(0, w)$ (red point, false vacuum) and $(v, 0)$ (blue point, true vacuum), are separated by a barrier resulting from the λ_{hs} term. This barrier is clearly illustrated in the middle panel, where the field values are taken along the green dashed line in the left panel. The barrier gives rise to a U-shaped $S_3(T)/T$, as depicted by the blue line in the right panel of Fig. 7. Additionally, we show the corresponding linear and quadratic approximations of $S_3(T)/T$. We again see the linear expansion fails to capture the shape of the complete expression.

To provide a comprehensive overview of the parameter space, we conducted a 2-dimensional scan for m_s and λ_{hs} while keeping λ_s as different fixed values, as depicted in the top panel of Fig. 8. In the top-left panel, we specifically plotted the parameter space for $f_{\text{pbh}} \in [10^{-100}, 1]$ and observed that it consists of narrow regions resembling “lines”. These “lines” have endpoints determined by ensuring the triviality bound [99]. It is well known that large scalar coupling constants are in general required to realize the FOPT. However, such large scalar coupling constants are strongly constrained by the triviality bound [100]. We take into account the constraint from the triviality bound by employing mass dependent beta functions [101]. We require that the Landau pole of the scalar couplings remains above 10 TeV to satisfy the triviality bound.

The top-right panel of Fig. 8 shows the details of the parameter space for $\lambda_s = 2$, near the vicinity of $m_s = 218.4$ GeV and $\lambda_{hs} = 1.106$. The PBH formation parameter space corresponds to strong GW production, and we have evaluated the corresponding GW spectra and verified that they are easily detected by the future LISA [102], TianQin [103], Taiji [104], and DECIGO [105] interferometers. Moreover, we illustrate the deviations in the

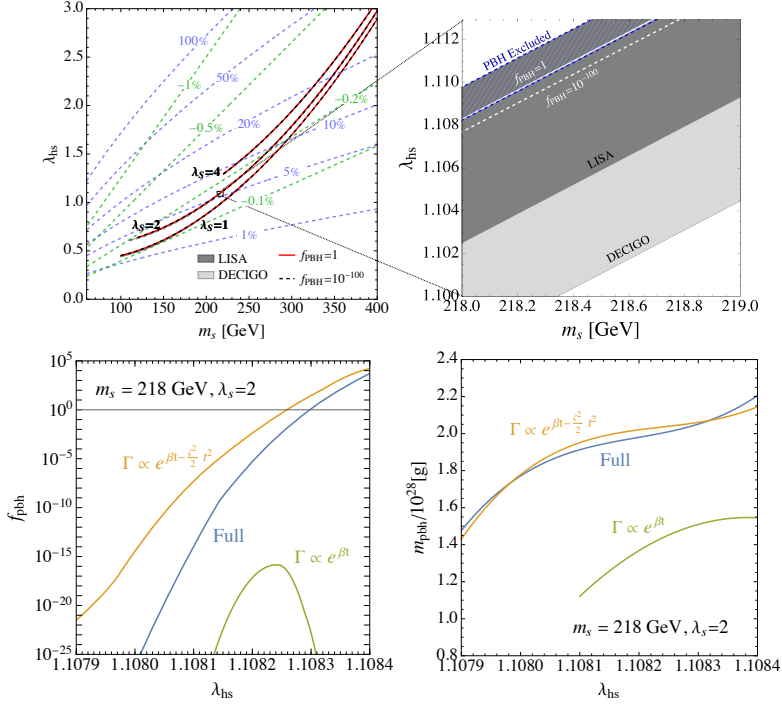


Figure 8. Top: the parameter space for PBH formation in the \mathbb{Z}_2 -symmetric xSM. Bottom-left (-right): The PBH fraction (mass) as a function of λ_{hs} for different treatments of $S(t)$, where $m_s = 218$ GeV and $\lambda_s = 2$ are fixed.

hhh and hWW/hZZ couplings as purple and green dashed contours, respectively. These deviations can be precisely measured at future collider experiments like HL-LHC [106], CEPC [107], ILC [108], and FCC-ee [109]. Those future collider experiments can offer complementary and correlated probes to this PBH formation mechanism.

In the bottom-left and -right panels of Fig. 8, we present the variations of f_{pbh} and m_{pbh} with respect to λ_{hs} , considering different treatments for $S(t)$ while keeping $m_s = 218$ GeV and $\lambda_s = 2$ fixed. We observe that the PBH fraction exhibits rapid changes as a function of λ_{hs} , primarily due to the significant influence of the barrier height on the probability of delayed vacuum decay. Conversely, the PBH mass $\sim 10^{28}$ g ($\sim 10^{-5} M_\odot$) changes gradually as it is predominantly determined by the temperature of the FOPT. It can be seen in the figure that the linear expansion fails to accurately describe the dynamics of PBH formation, as expected.

5 Conclusion

We explore the PBH formation through the delayed vacuum decay in the slow FOPTs, also known as the “late-blooming” mechanism, from a model-building perspective. We for the first time investigate this mechanism in models with zero-temperature potential barriers, taking the polynomial potential and the \mathbb{Z}_2 -symmetric xSM as two examples. Our findings reveal that a U-shaped Euclidean action significantly prolongs the phase transition, leading

to abundant PBH formation with sufficiently high barriers. Unlike models with classically conformal invariance [18–20], the FOPT in these models is moderate with an $\mathcal{O}(1)$ α parameter. Therefore, our study demonstrates a general type of particle models that can realize the PBH formation without requiring ultra-supercooling. The PBH abundance is highly sensitive to model parameters, which is a distinctive feature of this mechanism and has been demonstrated in previous literature [16–19]. Additionally, we explicitly show that the exponential nucleation approximation does not work in our models due to the U-shaped action, emphasizing the necessity for the full expression of the decay rate in particle-based studies.

Although our focus in this study is on particle models with zero-temperature barriers, the discussions presented in Section 2, especially in Section 2.2 regarding the validity of the exponential approximation, also have implications for more general models, including the classically conformal ones. In those models, where $S_3(T)/T \sim T^r$ with $r > 1$, satisfying Eq. (2.23) becomes challenging if one desires a small β/H_* to facilitate PBH formation. Consequently, the exponential approximation may also fail in PBH studies of such models, resulting in significant errors of several orders of magnitude. It is also important to note that for FOPTs characterized by long-lasting or ultra-supercooling regimes, it is necessary to verify the fulfillment of Eq. (2.21) to ensure the completion of the phase transition, which is not realized in some relevant literature.

Our work can be extended in several ways. While we have chosen $v_w = 1$ as a benchmark value, it is important to consider the friction force induced by plasma particles, which typically leads to bubble wall velocities smaller than 1 [110–115]. By varying v_w as different constants in our calculations, we find that lower values of v_w result in later percolation and larger PBH abundance, with differences spanning several orders of magnitude. Therefore, accurately determining the velocity within a specific model is crucial for deriving the PBH abundance. Different definitions of overdensity $\delta(t)$ exist in the literature. In our research, we adopt the definition given by Eq. (2.6), which leads to a decrease in overdensity after reaching its maximum value δ_{\max} . This is consistent with Refs. [14, 17]. However, an alternative definition of $\delta(t)$, as used in Ref. [11], is given by

$$\delta(t) = \frac{\rho_{\text{in}}(t)}{\rho_{\text{out}}(t)} \frac{a_{\text{in}}^4(t)}{a_{\text{out}}^4(t)} - 1,$$

which tends to be constant after reaching δ_{\max} . It would be interesting to further explore and compare these two definitions from a theoretical perspective. Furthermore, the finite temperature potential expression can be improved by including the full one-loop thermal corrections and beyond, and the calculation framework can be enhanced to incorporate more detailed considerations of PBH formation possibilities [15, 16], or by conducting numerical simulations of FOPTs [116, 117]. Given the sensitivity of PBH formation to FOPT features in this mechanism, a more comprehensive treatment is expected to significantly impact the PBH abundance and the viable parameter space of a given model. However, the key qualitative conclusions drawn from our research will remain unchanged, including the relationship between zero-temperature barriers and PBH formation, as well as the breakdown of the exponential approximation.

Acknowledgments

We would like to thank Ligong Bian, Jing Liu, and Shao-Jiang Wang for the very useful and inspiring discussions. K.-P. X. also thanks the hospitality of Osaka University where part of this work was performed, and Guang-Ze Fu for the great help on programming. The work of S. K. was supported in part by the JSPS KAKENHI Grant No. 20H00160 and No. 23K17691. M. T. was supported by the Iwanami Fujukai Foundation. K.-P. X. is supported by the National Science Foundation of China under Grant No. 12305108.

A FOPT dynamics under the exponential approximation

In this appendix, we derive the analytical results of the FOPT dynamics under the exponential approximation $\Gamma(t) \approx \Gamma_* e^{\beta(t-t_*)}$. Assume the FOPT is fast that $a(t)$ almost does not change during the transition, then the false vacuum fraction can be explicitly integrated out as

$$F(t) \approx \exp \left\{ -\frac{4\pi}{3} \int_{t_c}^t dt' \Gamma(t') \left(\int_{t'}^t dt'' v_w \right)^3 \right\} \approx \exp \left\{ -\frac{8\pi v_w^3}{3\beta^4/\Gamma_*} e^{\beta(t-t_*)} \right\}, \quad (\text{A.1})$$

where we have assumed $\beta(t-t_c) \gg 1$ and dropped the terms proportional to $e^{-\beta(t-t_c)}$ inside the exponent. Then the bubble density can be also explicitly derived as

$$n_b(t) \approx \int_{t_c}^t dt' F(t') \Gamma(t') \approx \left(\frac{\beta}{(8\pi)^{1/3} v_w} \right)^3 (1 - F(t)). \quad (\text{A.2})$$

Therefore, in the $t \rightarrow \infty$ limit we obtain $\bar{R}/[(8\pi)^{1/3} v_w] \rightarrow \beta^{-1}$, and hence $(8\pi)^{1/3} v_w/(H_* \bar{R})$ approaches β/H_* [118].

Now we would like to derive the (rough) relation between FOPT duration and β^{-1} . Rewriting Eq. (A.1) as

$$t - t_* = \beta^{-1} \log \left[-\frac{3}{8\pi v_w^3} \frac{\beta^4}{\Gamma_*} \log F(t) \right], \quad (\text{A.3})$$

and assuming the false vacuum volume fractions at t_2 and t_1 are F_2 and F_1 , respectively, we find

$$\Delta t \equiv t_2 - t_1 = \beta^{-1} \log \left(\frac{\log F_2}{\log F_1} \right). \quad (\text{A.4})$$

An appropriate definition of the FOPT duration is to set

$$F_2 = \eta, \quad F_1 = 1 - \eta, \quad (\text{A.5})$$

where η is a small positive number. This definition of Δt depends logarithmically on the parameter η . For $\eta = 10^{-2}$, 10^{-3} , and 10^{-4} , we obtain $\Delta t = 6.1 \beta^{-1}$, $8.8 \beta^{-1}$, and $11.4 \beta^{-1}$, respectively. Therefore, typically the FOPT duration $\Delta t \approx \mathcal{O}(10) \times \beta^{-1}$, consistent with the usual interpretation of β^{-1} in the exponential approximation.

References

- [1] B. Carr, K. Kohri, Y. Sendouda and J. Yokoyama, “Constraints on primordial black holes,” *Rept. Prog. Phys.* **84** (2021) 116902, [[2002.12778](#)].
- [2] A. M. Green and B. J. Kavanagh, “Primordial Black Holes as a dark matter candidate,” *J. Phys. G* **48** (2021) 043001, [[2007.10722](#)].
- [3] A. Escrivà, F. Kuhnel and Y. Tada, “Primordial Black Holes,” [2211.05767](#).
- [4] LISA COSMOLOGY WORKING GROUP collaboration, E. Bagui et al., “Primordial black holes and their gravitational-wave signatures,” [2310.19857](#).
- [5] S. W. Hawking, I. G. Moss and J. M. Stewart, “Bubble Collisions in the Very Early Universe,” *Phys. Rev. D* **26** (1982) 2681.
- [6] M. Lewicki and V. Vaskonen, “On bubble collisions in strongly supercooled phase transitions,” *Phys. Dark Univ.* **30** (2020) 100672, [[1912.00997](#)].
- [7] T. H. Jung and T. Okui, “Primordial black holes from bubble collisions during a first-order phase transition,” [2110.04271](#).
- [8] H. Kodama, M. Sasaki and K. Sato, “Abundance of Primordial Holes Produced by Cosmological First Order Phase Transition,” *Prog. Theor. Phys.* **68** (1982) 1979.
- [9] L. J. Hall and S. Hsu, “Cosmological Production of Black Holes,” *Phys. Rev. Lett.* **64** (1990) 2848–2851.
- [10] A. Kusenko, M. Sasaki, S. Sugiyama, M. Takada, V. Takhistov and E. Vitagliano, “Exploring Primordial Black Holes from the Multiverse with Optical Telescopes,” *Phys. Rev. Lett.* **125** (2020) 181304, [[2001.09160](#)].
- [11] J. Liu, L. Bian, R.-G. Cai, Z.-K. Guo and S.-J. Wang, “Primordial black hole production during first-order phase transitions,” *Phys. Rev. D* **105** (2022) L021303, [[2106.05637](#)].
- [12] K. Hashino, S. Kanemura and T. Takahashi, “Primordial black holes as a probe of strongly first-order electroweak phase transition,” *Phys. Lett. B* **833** (2022) 137261, [[2111.13099](#)].
- [13] K. Hashino, S. Kanemura, T. Takahashi and M. Tanaka, “Probing first-order electroweak phase transition via primordial black holes in the effective field theory,” *Phys. Lett. B* **838** (2023) 137688, [[2211.16225](#)].
- [14] S. He, L. Li, Z. Li and S.-J. Wang, “Gravitational Waves and Primordial Black Hole Productions from Gluodynamics,” [2210.14094](#).
- [15] K. Kawana, T. Kim and P. Lu, “PBH formation from overdensities in delayed vacuum transitions,” *Phys. Rev. D* **108** (2023) 103531, [[2212.14037](#)].
- [16] M. Lewicki, P. Toczek and V. Vaskonen, “Primordial black holes from strong first-order phase transitions,” *JHEP* **09** (2023) 092, [[2305.04924](#)].
- [17] Y. Gouttenoire and T. Volansky, “Primordial Black Holes from Supercooled Phase Transitions,” [2305.04942](#).
- [18] Y. Gouttenoire, “Primordial Black Holes from Conformal Higgs,” [2311.13640](#).
- [19] A. Salvio, “Pulsar Timing Arrays and Primordial Black Holes from a Supercool Phase Transition,” [2312.04628](#).

- [20] A. Conaci, L. Delle Rose, P. S. B. Dev and A. Ghoshal, “Slaying Axion-Like Particles via Gravitational Waves and Primordial Black Holes from Supercooled Phase Transition,” [2401.09411](#).
- [21] I. K. Banerjee and U. K. Dey, “Probing the origin of primordial black holes through novel gravitational wave spectrum,” *JCAP* **07** (2023) 024, [[2305.07569](#)].
- [22] I. K. Banerjee and U. K. Dey, “Gravitational Waves from Superradiance to Probe the Origin of Primordial Black Holes,” [2311.02876](#).
- [23] I. K. Banerjee and U. K. Dey, “Spinning Primordial Black Holes from First Order Phase Transition,” [2311.03406](#).
- [24] I. Baldes and M. O. Olea-Romacho, “Primordial black holes as dark matter: Interferometric tests of phase transition origin,” [2307.11639](#).
- [25] M. Lewicki, P. Toczek and V. Vaskonen, “Black holes and gravitational waves from slow phase transitions,” [2402.04158](#).
- [26] S. Balaji, M. Fairbairn and M. O. Olea-Romacho, “Magnetogenesis with gravitational waves and primordial black hole dark matter,” [2402.05179](#).
- [27] R. Jinno, J. Kume and M. Yamada, “Super-slow phase transition catalyzed by BHs and the birth of baby BHs,” [2310.06901](#).
- [28] M. M. Flores, A. Kusenko and M. Sasaki, “Revisiting formation of primordial black holes in a supercooled first-order phase transition,” [2402.13341](#).
- [29] T. D. Lee and Y. Pang, “Fermion Soliton Stars and Black Holes,” *Phys. Rev. D* **35** (1987) 3678.
- [30] C. Gross, G. Landini, A. Strumia and D. Teresi, “Dark Matter as dark dwarfs and other macroscopic objects: multiverse relics?,” *JHEP* **09** (2021) 033, [[2105.02840](#)].
- [31] M. J. Baker, M. Breitbach, J. Kopp and L. Mittnacht, “Primordial Black Holes from First-Order Cosmological Phase Transitions,” [2105.07481](#).
- [32] M. J. Baker, M. Breitbach, J. Kopp and L. Mittnacht, “Detailed Calculation of Primordial Black Hole Formation During First-Order Cosmological Phase Transitions,” [2110.00005](#).
- [33] K. Kawana and K.-P. Xie, “Primordial black holes from a cosmic phase transition: The collapse of Fermi-balls,” *Phys. Lett. B* **824** (2022) 136791, [[2106.00111](#)].
- [34] P. Huang and K.-P. Xie, “Primordial black holes from an electroweak phase transition,” *Phys. Rev. D* **105** (2022) 115033, [[2201.07243](#)].
- [35] K. Kawana, P. Lu and K.-P. Xie, “First-order phase transition and fate of false vacuum remnants,” *JCAP* **10** (2022) 030, [[2206.09923](#)].
- [36] P. Lu, K. Kawana and A. Kusenko, “Late-forming primordial black holes: Beyond the CMB era,” *Phys. Rev. D* **107** (2023) 103037, [[2210.16462](#)].
- [37] D. Marfatia and P.-Y. Tseng, “Correlated signals of first-order phase transitions and primordial black hole evaporation,” *JHEP* **08** (2022) 001, [[2112.14588](#)].
- [38] D. Marfatia and P.-Y. Tseng, “Boosted dark matter from primordial black holes produced in a first-order phase transition,” *JHEP* **04** (2023) 006, [[2212.13035](#)].
- [39] P.-Y. Tseng and Y.-M. Yeh, “511 keV line and primordial black holes from first-order phase transitions,” *JCAP* **08** (2023) 035, [[2209.01552](#)].

- [40] K.-P. Xie, “Pinning down the primordial black hole formation mechanism with gamma-rays and gravitational waves,” *JCAP* **06** (2023) 008, [[2301.02352](#)].
- [41] J. T. Acuña and P.-Y. Tseng, “Probing primordial black holes from a first order phase transition through pulsar timing and gravitational wave signals,” *JHEP* **08** (2023) 117, [[2304.10084](#)].
- [42] M. Lewicki, K. Mürsepp, J. Pata, M. Vasar, V. Vaskonen and H. Veermäe, “Dynamics of false vacuum bubbles with trapped particles,” *Phys. Rev. D* **108** (2023) 036023, [[2305.07702](#)].
- [43] P.-J. Chen and P.-Y. Tseng, “Type Ia supernovae induced by primordial black holes from dark first-order phase transition,” *JHEAp* **39** (2023) 106–113, [[2305.14399](#)].
- [44] T. Kim, P. Lu, D. Marfatia and V. Takhistov, “Regurgitated Dark Matter,” [2309.05703](#).
- [45] T. C. Gehrman, B. Shams Es Haghi, K. Sinha and T. Xu, “Recycled Dark Matter,” [2310.08526](#).
- [46] L. Del Grosso, P. Pani and A. Urbano, “Compact objects in and beyond the Standard Model from non-perturbative vacuum scalarization,” [2401.06716](#).
- [47] D. Borah, S. Jyoti Das and I. Saha, “Dark matter from phase transition generated PBH evaporation with gravitational waves signatures,” [2401.12282](#).
- [48] A. Mazumdar and G. White, “Review of cosmic phase transitions: their significance and experimental signatures,” *Rept. Prog. Phys.* **82** (2019) 076901, [[1811.01948](#)].
- [49] J. Ellis, M. Lewicki and J. M. No, “On the Maximal Strength of a First-Order Electroweak Phase Transition and its Gravitational Wave Signal,” *JCAP* **04** (2019) 003, [[1809.08242](#)].
- [50] A. D. Linde, “Decay of the False Vacuum at Finite Temperature,” *Nucl. Phys. B* **216** (1983) 421.
- [51] I. Musco, J. C. Miller and L. Rezzolla, “Computations of primordial black hole formation,” *Class. Quant. Grav.* **22** (2005) 1405–1424, [[gr-qc/0412063](#)].
- [52] T. Harada, C.-M. Yoo and K. Kohri, “Threshold of primordial black hole formation,” *Phys. Rev. D* **88** (2013) 084051, [[1309.4201](#)].
- [53] V. A. Berezin, V. A. Kuzmin and I. I. Tkachev, “THIN WALL VACUUM DOMAINS EVOLUTION,” *Phys. Lett. B* **120** (1983) 91–96.
- [54] S. K. Blau, E. I. Guendelman and A. H. Guth, “The Dynamics of False Vacuum Bubbles,” *Phys. Rev. D* **35** (1987) 1747.
- [55] J. Garriga, A. Vilenkin and J. Zhang, “Black holes and the multiverse,” *JCAP* **02** (2016) 064, [[1512.01819](#)].
- [56] H. Deng, “Primordial black hole formation by vacuum bubbles. Part II,” *JCAP* **09** (2020) 023, [[2006.11907](#)].
- [57] B. J. Carr, “The Primordial black hole mass spectrum,” *Astrophys. J.* **201** (1975) 1–19.
- [58] PARTICLE DATA GROUP collaboration, R. L. Workman et al., “Review of Particle Physics,” *PTEP* **2022** (2022) 083C01.
- [59] C. Caprini et al., “Detecting gravitational waves from cosmological phase transitions with LISA: an update,” *JCAP* **03** (2020) 024, [[1910.13125](#)].

- [60] H.-K. Guo, K. Sinha, D. Vagie and G. White, “The benefits of diligence: how precise are predicted gravitational wave spectra in models with phase transitions?,” *JHEP* **06** (2021) 164, [[2103.06933](#)].
- [61] P. Athron, C. Balázs, A. Fowlie, L. Morris and L. Wu, “Cosmological phase transitions: From perturbative particle physics to gravitational waves,” *Prog. Part. Nucl. Phys.* **135** (2024) 104094, [[2305.02357](#)].
- [62] M. D. Rintoul and S. Torquato, “Precise determination of the critical threshold and exponents in a three-dimensional continuum percolation model,” *Journal of physics a: mathematical and general* **30** (1997) L585.
- [63] J. Ellis, M. Lewicki, J. M. No and V. Vaskonen, “Gravitational wave energy budget in strongly supercooled phase transitions,” *JCAP* **06** (2019) 024, [[1903.09642](#)].
- [64] X. Wang, F. P. Huang and X. Zhang, “Phase transition dynamics and gravitational wave spectra of strong first-order phase transition in supercooled universe,” *JCAP* **05** (2020) 045, [[2003.08892](#)].
- [65] M. S. Turner, E. J. Weinberg and L. M. Widrow, “Bubble nucleation in first order inflation and other cosmological phase transitions,” *Phys. Rev. D* **46** (1992) 2384–2403.
- [66] M. Dine, R. G. Leigh, P. Y. Huet, A. D. Linde and D. A. Linde, “Towards the theory of the electroweak phase transition,” *Phys. Rev. D* **46** (1992) 550–571, [[hep-ph/9203203](#)].
- [67] A. Megevand and S. Ramirez, “Bubble nucleation and growth in very strong cosmological phase transitions,” *Nucl. Phys. B* **919** (2017) 74–109, [[1611.05853](#)].
- [68] R.-G. Cai, M. Sasaki and S.-J. Wang, “The gravitational waves from the first-order phase transition with a dimension-six operator,” *JCAP* **08** (2017) 004, [[1707.03001](#)].
- [69] NANOGrav collaboration, G. Agazie et al., “The NANOGrav 15 yr Data Set: Evidence for a Gravitational-wave Background,” *Astrophys. J. Lett.* **951** (2023) L8, [[2306.16213](#)].
- [70] H. Xu et al., “Searching for the Nano-Hertz Stochastic Gravitational Wave Background with the Chinese Pulsar Timing Array Data Release I,” *Res. Astron. Astrophys.* **23** (2023) 075024, [[2306.16216](#)].
- [71] EPTA, INPTA: collaboration, J. Antoniadis et al., “The second data release from the European Pulsar Timing Array - III. Search for gravitational wave signals,” *Astron. Astrophys.* **678** (2023) A50, [[2306.16214](#)].
- [72] D. J. Reardon et al., “Search for an Isotropic Gravitational-wave Background with the Parkes Pulsar Timing Array,” *Astrophys. J. Lett.* **951** (2023) L6, [[2306.16215](#)].
- [73] NANOGrav collaboration, A. Afzal et al., “The NANOGrav 15 yr Data Set: Search for Signals from New Physics,” *Astrophys. J. Lett.* **951** (2023) L11, [[2306.16219](#)].
- [74] G. Hobbs et al., “The international pulsar timing array project: using pulsars as a gravitational wave detector,” *Class. Quant. Grav.* **27** (2010) 084013, [[0911.5206](#)].
- [75] A. Weltman et al., “Fundamental physics with the Square Kilometre Array,” *Publ. Astron. Soc. Austral.* **37** (2020) e002, [[1810.02680](#)].
- [76] C. Han, K.-P. Xie, J. M. Yang and M. Zhang, “Self-interacting dark matter implied by nano-Hertz gravitational waves,” [2306.16966](#).
- [77] S.-P. Li and K.-P. Xie, “Collider test of nano-Hertz gravitational waves from pulsar timing arrays,” *Phys. Rev. D* **108** (2023) 055018, [[2307.01086](#)].

- [78] E. Megias, G. Nardini and M. Quiros, “Pulsar timing array stochastic background from light Kaluza-Klein resonances,” *Phys. Rev. D* **108** (2023) 095017, [2306.17071].
- [79] K. Fujikura, S. Girmohanta, Y. Nakai and M. Suzuki, “NANOGrav signal from a dark conformal phase transition,” *Phys. Lett. B* **846** (2023) 138203, [2306.17086].
- [80] L. Zu, C. Zhang, Y.-Y. Li, Y.-C. Gu, Y.-L. S. Tsai and Y.-Z. Fan, “Mirror QCD phase transition as the origin of the nanohertz Stochastic Gravitational-Wave Background,” [2306.16769](#).
- [81] P. Athron, A. Fowlie, C.-T. Lu, L. Morris, L. Wu, Y. Wu et al., “Can supercooled phase transitions explain the gravitational wave background observed by pulsar timing arrays?,” [2306.17239](#).
- [82] S. Jiang, A. Yang, J. Ma and F. P. Huang, “Implication of nano-Hertz stochastic gravitational wave on dynamical dark matter through a first-order phase transition,” [2306.17827](#).
- [83] A. Addazi, Y.-F. Cai, A. Marciano and L. Visinelli, “Have pulsar timing array methods detected a cosmological phase transition?,” [2306.17205](#).
- [84] T. Bringmann, P. F. Depta, T. Konstandin, K. Schmidt-Hoberg and C. Tasillo, “Does NANOGrav observe a dark sector phase transition?,” *JCAP* **11** (2023) 053, [2306.09411].
- [85] E. Madge, E. Morgante, C. Puchades-Ibáñez, N. Ramberg, W. Ratzinger, S. Schenk et al., “Primordial gravitational waves in the nano-Hertz regime and PTA data — towards solving the GW inverse problem,” *JHEP* **10** (2023) 171, [2306.14856].
- [86] Z.-C. Chen, S.-L. Li, P. Wu and H. Yu, “NANOGrav hints for first-order confinement-deconfinement phase transition in different QCD-matter scenarios,” [2312.01824](#).
- [87] S. He, L. Li, S. Wang and S.-J. Wang, “Constraints on holographic QCD phase transitions from PTA observations,” [2308.07257](#).
- [88] H. An, B. Su, H. Tai, L.-T. Wang and C. Yang, “Phase transition during inflation and the gravitational wave signal at pulsar timing arrays,” [2308.00070](#).
- [89] L. Bian, S. Ge, J. Shu, B. Wang, X.-Y. Yang and J. Zong, “Gravitational wave sources for Pulsar Timing Arrays,” [2307.02376](#).
- [90] J. Ellis, M. Fairbairn, G. Franciolini, G. Hütsi, A. Iovino, M. Lewicki et al., “What is the source of the PTA GW signal?,” [2308.08546](#).
- [91] T. Ghosh, A. Ghoshal, H.-K. Guo, F. Hajkarim, S. F. King, K. Sinha et al., “Did we hear the sound of the Universe boiling? Analysis using the full fluid velocity profiles and NANOGrav 15-year data,” [2307.02259](#).
- [92] Y. Xiao, J. M. Yang and Y. Zhang, “Implications of Nano-Hertz Gravitational Waves on Electroweak Phase Transition in the Singlet Dark Matter Model,” [2307.01072](#).
- [93] J. McDonald, “Electroweak baryogenesis and dark matter via a gauge singlet scalar,” *Phys. Lett. B* **323** (1994) 339–346.
- [94] S. Profumo, M. J. Ramsey-Musolf and G. Shaughnessy, “Singlet Higgs phenomenology and the electroweak phase transition,” *JHEP* **08** (2007) 010, [0705.2425].
- [95] J. R. Espinosa, T. Konstandin and F. Riva, “Strong Electroweak Phase Transitions in the Standard Model with a Singlet,” *Nucl. Phys. B* **854** (2012) 592–630, [1107.5441].

- [96] K.-P. Xie, “Lepton-mediated electroweak baryogenesis, gravitational waves and the 4τ final state at the collider,” *JHEP* **02** (2021) 090, [[2011.04821](#)].
- [97] L. Bian, Y. Wu and K.-P. Xie, “Electroweak phase transition with composite Higgs models: calculability, gravitational waves and collider searches,” *JHEP* **12** (2019) 028, [[1909.02014](#)].
- [98] C. L. Wainwright, “CosmoTransitions: Computing Cosmological Phase Transition Temperatures and Bubble Profiles with Multiple Fields,” *Comput. Phys. Commun.* **183** (2012) 2006–2013, [[1109.4189](#)].
- [99] M. Lindner, “Implications of Triviality for the Standard Model,” *Z. Phys. C* **31** (1986) 295.
- [100] S. Kanemura, E. Senaha, T. Shindou and T. Yamada, “Electroweak phase transition and Higgs boson couplings in the model based on supersymmetric strong dynamics,” *JHEP* **05** (2013) 066, [[1211.5883](#)].
- [101] S. Kanemura and Y. Mura, “New application of the mass-dependent analysis for renormalization group equation to extended Higgs models,” [2310.15622](#).
- [102] LISA collaboration, P. Amaro-Seoane et al., “Laser Interferometer Space Antenna,” [1702.00786](#).
- [103] TIANQIN collaboration, J. Luo et al., “TianQin: a space-borne gravitational wave detector,” *Class. Quant. Grav.* **33** (2016) 035010, [[1512.02076](#)].
- [104] W.-R. Hu and Y.-L. Wu, “The Taiji Program in Space for gravitational wave physics and the nature of gravity,” *Natl. Sci. Rev.* **4** (2017) 685–686.
- [105] S. Kawamura et al., “The Japanese space gravitational wave antenna: DECIGO,” *Class. Quant. Grav.* **28** (2011) 094011.
- [106] M. Cepeda et al., “Report from Working Group 2: Higgs Physics at the HL-LHC and HE-LHC,” *CERN Yellow Rep. Monogr.* **7** (2019) 221–584, [[1902.00134](#)].
- [107] F. An et al., “Precision Higgs physics at the CEPC,” *Chin. Phys. C* **43** (2019) 043002, [[1810.09037](#)].
- [108] P. Bambade et al., “The International Linear Collider: A Global Project,” [1903.01629](#).
- [109] FCC collaboration, A. Abada et al., “FCC-ee: The Lepton Collider: Future Circular Collider Conceptual Design Report Volume 2,” *Eur. Phys. J. ST* **228** (2019) 261–623.
- [110] M. Lewicki, M. Merchand and M. Zych, “Electroweak bubble wall expansion: gravitational waves and baryogenesis in Standard Model-like thermal plasma,” *JHEP* **02** (2022) 017, [[2111.02393](#)].
- [111] B. Laurent and J. M. Cline, “First principles determination of bubble wall velocity,” *Phys. Rev. D* **106** (2022) 023501, [[2204.13120](#)].
- [112] S.-J. Wang and Z.-Y. Yuwen, “Hydrodynamic backreaction force of cosmological bubble expansion,” *Phys. Rev. D* **107** (2023) 023501, [[2205.02492](#)].
- [113] J.-C. Wang, Z.-Y. Yuwen, Y.-S. Hao and S.-J. Wang, “General backreaction force of cosmological bubble expansion,” [2310.07691](#).
- [114] W.-Y. Ai, B. Laurent and J. van de Vis, “Model-independent bubble wall velocities in local thermal equilibrium,” *JCAP* **07** (2023) 002, [[2303.10171](#)].
- [115] W.-Y. Ai, X. Nagels and M. Vanvlasselaer, “Criterion for ultra-fast bubble walls: the impact of hydrodynamic obstruction,” [2401.05911](#).

- [116] Y. Di, J. Wang, R. Zhou, L. Bian, R.-G. Cai and J. Liu, “Magnetic Field and Gravitational Waves from the First-Order Phase Transition,” *Phys. Rev. Lett.* **126** (2021) 251102, [[2012.15625](#)].
- [117] Z. Zhao, Y. Di, L. Bian and R.-G. Cai, “Probing the electroweak symmetry breaking history with gravitational waves,” *JHEP* **10** (2023) 158, [[2204.04427](#)].
- [118] K. Enqvist, J. Ignatius, K. Kajantie and K. Rummukainen, “Nucleation and bubble growth in a first order cosmological electroweak phase transition,” *Phys. Rev. D* **45** (1992) 3415–3428.